tvst

Article

Comparisons Among Optical Coherence Tomography and Fundus Autofluorescence Modalities as Measurements of Atrophy in *ABCA4*-Associated Disease

Rait Parmann[1], Stephen H. Tsang[1,2], Jana Zernant[1], Rando Allikmets[1,2], Vivienne C. Greenstein[1], and Janet R. Sparrow[1,2]

[1] Department of Ophthalmology, Harkness Eye Institute, Columbia University, New York, NY, USA
[2] Department of Pathology and Cell Biology, Columbia University Medical Center, New York, NY, USA

Correspondence: Janet R. Sparrow, Department of Ophthalmology, Columbia University, New York, NY 10032, USA.
e-mail: jrs88@columbia.edu

Received: June 4, 2021
Accepted: November 22, 2021
Published: January 28, 2022

Keywords: hypertransmission; near-infrared fundus autofluorescence; optical coherence tomography; retina; retinal pigment epithelium; scanning laser ophthalmoscopy; short-wavelength fundus autofluorescence

Citation: Parmann R, Tsang SH, Zernant J, Allikmets R, Greenstein VC, Sparrow JR. Comparisons among optical coherence tomography and fundus autofluorescence modalities as measurements of atrophy in *ABCA4*-associated disease. Transl Vis Sci Technol. 2022;11(1):36, https://doi.org/10.1167/tvst.11.1.36

Purpose: In *ABCA4*-associated retinopathy, central atrophy was assessed by spectral domain optical coherence tomography (SD-OCT) and by short-wavelength (SW-AF) and near-infrared (NIR-AF) autofluorescence.

Methods: Patients exhibited a central atrophic lesion characterized by hypoautofluorescence (hypoAF) surrounded either by hyperautofluorescent (hyperAF) rings in both AF images (group 1, 4 patients); or a hyperAF ring in SW-AF but not in NIR-AF images (group 2, 11 patients); or hyperAF rings in neither AF images (group 3, 11 patients). Choroidal hypertransmission and widths of ellipsoid zone (EZ) loss were measured in foveal SD-OCT scans, and in AF images hypoAF and total hypo+hyperAF widths were measured along the same axis. Bland-Altman and repeated measures analysis of variance with Tukey post hoc were applied.

Results: For all groups, hypertransmission widths were significantly smaller than EZ loss widths. In Groups 1 and 2, hypertransmission width was not significantly different than SW-hypoAF width, but hypertransmission was narrower than the width of SW-hypo+hyperAF (groups 1, 2) and NIR-hypo+hyperAF (group 1). In group 3, the hypertransmission width was also significantly less than the width of SW-hypoAF and NIR-hypoAF. The EZ loss widths were not significantly different than measurements of total lesion size, the latter being the widths of SW-hypo+hyperAF and NIR-hypo+hyperAF (group 1); widths of NIR-hypoAF and SW-hypo+hyperAF (group 2); and widths of NIR-hypoAF and SW-hypoAF (group 3).

Conclusions: Hypertransmission and SW-hypoAF (except when reflecting total lesion width) underestimate lesion size detected by EZ loss, SW-hypoAF+hyperAF, and NIR-hypo+hyperAF.

Translational Relevance: The findings are significant to the selection of outcome measures in clinical studies.

Introduction

The monogenic retinopathy associated with disease-causing variants in *ABCA4* begins in the central macula and typically expands outwardly. Central vision loss is often evident in adolescence or in the young adult, but disease can also manifest at earlier and later ages.[1] A broad range of clinical phenotypes are associated with disease causing variants in *ABCA4*[2,3] and phenotype-genotype correlations are made difficult by the allelic heterogeneity of *ABCA4*-related disease.[4] En face fundus features of *ABCA4*-related disease vary from a circular area of atrophy confined to central macula (bull's eye maculopathy) to retina-wide disease and can include foveal or peripapillary sparing.[1,5] Other phenotypes consistent with *ABCA4*-associated disease include increased short-wavelength autofluorescence (SW-AF) (488 nm excitation) attributable to accelerated

accumulation of bisretinoid lipofuscin[6–9] and the presence of bright autofluorescent fundus flecks.[10–13] Natural history studies of *ABCA4*-associated disease have also relied on spectral-domain optical coherence tomography (SD-OCT) and microperimetry.[14] In some cases, the near-infrared autofluorescence (NIR-AF) signal originating primarily in retinal pigment epithelium (RPE) melanin (787 excitation) (with some contribution from choroidal melanocytes)[15,16] has been particularly informative. For instance, the hypoautofluorescence (hypoAF) of flecks in NIR-AF images together with the extension of hyperreflective flecks anteriorly through photoreceptor attributable bands in SD-OCT scans and their position anterior to RPE/Bruch's membrane in en face OCT images[13,17–19] indicates that the hyperautofluorescence of fundus flecks in *ABCA4*-associated disease originates from augmented bisretinoid lipofuscin formation in impaired photoreceptor cells rather than bloated RPE cells.

Monitoring disease progression in *ABCA4*-associated retinopathy has relied primarily on the measurement of the change in area of central atrophic lesions visible as hypoAF in SW-AF images, central loss of the band attributable to the ellipsoid zone (EZ) in SD-OCT scans, the decline in best-corrected visual acuity, and the loss of visual sensitivity as measured by microperimetry.[14,17,20–28]

Areas of atrophy in *ABCA4*-related retinopathy are also characterized by sub-RPE hypertransmission of SD-OCT signal. Hypertransmission in standard OCT B-scans is typically recognized as intermittent lines of increased intensity (bar-coding) that extend posterior to RPE/Bruch's membrane and are caused by reduced or loss of melanin-induced reflectance of light in association with attenuation or disruption of the RPE-Bruch's membrane layer.[29]

SD-OCT findings related to EZ loss in *ABCA4*-related retinopathy have been compared to AF findings in previous qualitative and quantitative studies.[18,27,30] Here, we have measured the width of sub-RPE hypertransmission in horizontal SD-OCT B scans through the fovea and compared this metric to the width of RPE atrophy measured in en face SW-AF and NIR-AF images and to the width of EZ loss in the SD-OCT B scans.

Methods

This was a retrospective observational study of 26 patients (52 eyes, 9 female). All patients were diagnosed with recessive Stargardt disease (STGD1) confirmed by sequencing of the *ABCA4* gene. Patients underwent a complete ophthalmic examination including fundoscopy and measurement of the best-corrected visual acuity. Clinical, demographic and genetic characteristics of the study cohort are summarized in Table 1.

All patients were enrolled under approval by the Columbia University Medical Center Institutional Review Board, and all procedures adhered to tenets set out in the Declaration of Helsinki. Study inclusion criteria were clinical and genetic diagnosis of *ABCA4*-associated maculopathy and the availability of high quality NIR-AF, SW-AF and SD-OCT images (OCT quality index >30dB). Patients with widespread atrophy (measuring more than half of the diameter of the macular area) were excluded.

Pupils were dilated with 1% tropicamide and 2.5% phenylephrine before imaging. Spectralis HRA+OCT (Heidelberg Engineering, Heidelberg, Germany) was used to acquire conventional SW-AF images (480-nm excitation, 30° × 30° field, minimum 20 frames per image) saved in ART normalized mode. Horizontal SD-OCT scans (9 mm, 870 nm) were also obtained with corresponding near infrared reflectance (IR-R) (820 nm) fundus images. To obtain the highest signal-to-noise ratio for AF and OCT images the eye-tracking function was used. An HRA2 (Heidelberg Engineering) was used with the indocyanine-green angiography mode (787 nm excitation, 30° × 30° field) to capture NIR-AF images and averaging of up to 100 single frames in normalized mode for high-quality images.

Because of the clinical heterogeneity of STGD1, patients were divided into three groups based on the phenotypic presentations in SW-AF and NIR-AF images: (1) a central hypoAF lesion surrounded by a hyperautofluorescent (hyperAF) ring in both SW-AF and NIR-AF images; (2) a central hypoAF lesion surrounded by a hyperAF ring in SW-AF but not in NIR-AF images; and (3) a central hypoAF lesion with no hyperAF ring in either image modality (Fig. 1). Foveal sparing was not addressed.

All measurements were acquired by using the built-in Measure Distance tool in the Heidelberg Eye Explorer software (Heidelberg Engineering). A horizontal SD-OCT scan through the fovea was chosen, and two variables were measured: the horizontal length of continuous EZ loss and the width of the SD-OCT signal hypertransmission into the sub-RPE region. In SW-AF and NIR-AF images the measurements were acquired along the same horizontal axis through the fovea as in the SD-OCT scan. The diameter of the central area of reduced autofluorescence (SW-hypoAF, NIR-hypoAF) was also measured. Additionally, in the presence of a hyperAF ring immediately

Table 1. Patient Demographic, Clinical, and Genetic Data

ID	Gender	Age (y)	Race/Ethnicity	BCVA (logMar) OD	BCVA (logMar) OS	Group	ABCA4 Variants
1	F	22	White	0.7	0.8	3	c.2915C>A p.(Thr972Asn); c.6079C>T p.(Leu2027Phe)
2	F	18	White	0.8	0.8	2	c.3322C>T p.(Arg1108Cys); c.4234C>T p.(Gln1412*)
3	F	58	White	0.6	0.6	3	c.5603A>T p.(Asn1868Ile); c.6229C>T p.(Arg2077Trp)
4	M	26	White	0.5	0.5	2	c.161G>A p.(Cys54Tyr); c.5196+1137G>A p.[=,Met1733Glufs*78]
5	M	18	White	1.3	1.3	3	c.[1622T>C;3113C>T] p.([Leu541Pro;Ala1038Val]); c.5603A>T p.(Asn1868Ile)
6	F	30	White/Indian	0.7	0.6	1	c.634C>T p.(Arg212Cys); c.5882G>A p.(Gly1961Glu)
7	F	31	African American	0.9	0.9	2	c.2971G>C p.(Gly991Arg); c.3413T>C p.(Leu1138Pro)
8	F	17	White	0.9	0.7	2	c.4139C>T p.(Pro1380Leu); c.5714+5G>A p.[=,Glu1863Leufs*33]
9	M	30	White	0.3	0.3	2	c.3007C>T p.(Gln1003*); c.[3758C>T;5882G>A] p.([Thr1253Met;Gly1961Glu])
10	M	13	White	1.3	1.3	3	c.[1622T>C;3113C>T] p.([Leu541Pro;Ala1038Val]); c.5603A>T p.(Asn1868Ile)
11	M	14	White	0.4	0.9	3	c.2918+5G>A p.(?); c.2966T>C p.(Val989Ala)
12	M	16	White	0.7	0.9	2	c.3292C>T p.(Arg1098Cys); c.[5461-10T>C;5603A>T] p.(Thr1821Aspfs*6)
13	F	39	White	0.3	0.8	3	c.5351T>G p.(Leu1784Arg); c.6449G>A p.(Cys2150Tyr)
14	M	17	White	0.4	0.6	1	c.1844T>C p.(Val615Ala); c.5882G>A p.(Gly1961Glu)
15	F	23	White	0.7	0.6	1	c.5044_5058delGTTGCCATCTGCGTG p.(Val1682_Val1686del); c.5882G>A p.(Gly1961Glu)
16	M	33	White	0.2	0.3	2	c.4947delC p.(Glu1650fs*12); c.5882G>A p.(Gly1961Glu)
17	M	18	White	0.7	0.7	2	c.[2588G>C;5603A>T] p.([Gly863Ala,Gly863del;Asn1868Ile]); c.5316G>A p.(Trp1772*)
18	M	13	White	0.8	0.8	2	c.[1622T>C;3113C>T] p.([Leu541Pro;Ala1038Val]); c.6079C>T p.(Leu2027Phe)
19	M	18	White	0.3	0.4	3	c.[1622T>C;3113C>T] p.([Leu541Pro;Ala1038Val]); c.6079C>T p.(Leu2027Phe)
20	M	33	Indian	0.6	0.5	1	c.1957C>T p.(Arg653Cys); c.5882G>A p.(Gly1961Glu)
21	M	38	Indian	0.6	0.8	2	c.859-9T>C p.([=,Phe287_Arg452del]); c.859-9T>C p.([=,Phe287_Arg452del])
22	M	52	White	0.2	0.2	3	c.1522C>T p.(Arg508Cys); c.4224G>A p.(Trp1408*)
23	F	37	White	0.9	0.9	3	c.4139C>T p.(Pro1380Leu); c.5882G>A p.(Gly1961Glu)
24*	M	33	White	0.5	0.3	3	c.[3758C>T;5882G>A] p.([Thr1253Met;Gly1961Glu]); nd
25	M	28	White	0.6	0.6	3	c.4139C>T p.(Pro1380Leu); c.5882G>A p.(Gly1961Glu)
26	M	28	White	0.9	0.9	2	c.[5461-10T>C;5603A>T] p.(Thr1821Aspfs*6); c.5882G>A p.(Gly1961Glu)

BCVA, best corrected visual acuity.
*One disease-causing allele identified.

encircling the central hypoAF, the entire diameter of abnormal AF was measured (SW-hypo+hyperAF, NIR-hypo+hyperAF). Two of the authors (R.P. and V.G.) analyzed the images independently; interoperator reliability of the intraclass correlation coefficients (ICC) and their 95% confidence intervals (CI) was calculated using Microsoft Office Excel Analysis ToolPak (Microsoft, Redmond, WA, USA). The statistical analyses involving Bland-Altman plots and repeated measures analysis of variance (ANOVA) followed by the Tukey HSD post hoc test were performed using the GraphPad Prism 8 software (GraphPad Software, San Diego, CA, USA).

Results

Patients were grouped based on phenotypic features expressed in the SW-AF and NIR-AF images (Fig. 1). Group 1 consisted of patients (four patients, eight eyes) with a central hypoAF lesion surrounded by a hyperAF ring in both SW-AF and NIR-AF images. Group 2 comprised patients (11 patients, 22 eyes) exhibiting a central hypoAF lesion with a hyperAF ring surrounding the hypoAF central lesion in SW-AF but not in NIR-AF images. In Group 3 (11 patients, 22 eyes) were patients exhibiting a central hypoAF lesion without surrounding hyperAF rings.

Images from patient (P 14) (Fig. 2), are representative of group 1. The central lesion is readily detected in the SD-OCT scan by posterior hypertransmission of the SD-OCT signal into the choroid (Fig. 2A). In SW-AF and NIR-AF images the central lesion presents as hypoAF surrounded by hyperAF in both modalities (Figs. 2B, 2C). Foveal sparing is evident in the SD-OCT scan and in the *en face* images. The nasal and temporal borders of EZ loss (vertical red dashed lines in Fig. 2A) are situated outside the border of hypertransmission (vertical blue dashed lines in Fig. 2A). The width of EZ loss is greater than the width of the central hypoAF zone in NIR- and SW-AF images but similar to the combined width of the hypo+hyperAF region in SW- and NIR-AF images. The central lesion in Figure 3 (P9, Group 2) is similarly evidenced by hypoAF in both SW- and NIR-AF images, but an outer ring of hyperAF is present only in the SW-AF image; a ring is not present in the NIR-AF image. It is worth noting that the zone of brightness extending within a central area of 8° in diameter, caused by higher melanin optical density, can make it difficult to distinguish the normal brightness from abnormal hyperNIR-AF. Again, the limits of EZ loss (red vertical dashed lines) in the SD-OCT scan are positioned outside the zone of hypertransmission (blue vertical dashed lines) (Fig. 3 A). The region of hypoAF is also distinctly larger in the NIR-AF than in SW-AF image (Figs. 3B, 3C). Figure 4 presents

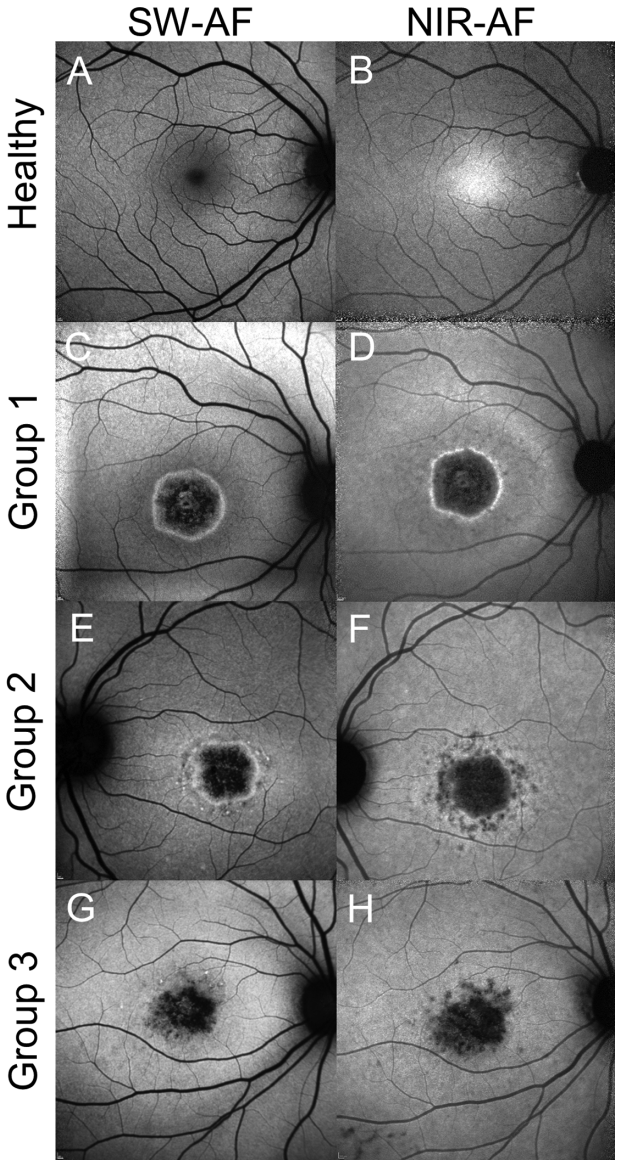

Figure 1. Phenotypes in SW-AF (A, C, E, G) and NIR-AF (B, D, F, H) images. (A, B) Images acquired from a healthy eye (age 32). (C, D) group 1 (P6). Central lesion of hypoautofluorescence (hypoAF) surrounded by hyperautofluorescent (hyperAF) rings in SW-AF and NIR-AF images. (E, F) Group 2 (P7). Central lesion of hypoAF surrounded by hyperAF only in the SW-AF image. (G, H) Group 3 (P13). Central hypoAF lesion is in SW-AF and NIR-AF images.

representative images obtained from a patient assigned to Group 3. The central hypoAF lesion in Figure 4 (P3, group 3) is uniformly darkened in the NIR-AF image (Fig. 4C) and mottled in the SW-AF image (Fig. 4B). In neither modality is there a hyperAF ring surrounding the central hypoAF lesion. In agreement with Groups 1 and 2, the width of EZ loss (vertical red dashed lines) is greater than the zone of hypertransmission (blue vertical dashed lines) in the SD-OCT scan (Fig. 4A). The hyperAF flecks in the SW-AF image (Fig. 4B white arrow) present as darkened puncta in the NIR-AF image and as hyper-reflective lesions in the SD-OCT scan. This fleck lesion extends through the interdigitation zone (IZ) and EZ bands of photoreceptor cell attributable layers and is associated anteriorly with outer nuclear layer thinning.

To investigate and visualize relationships among the metrics, we tested for equivalence using the Bland-Altman method, in which the difference between two measurements was graphed as a function of the average of the two measurements in a scatter plot (Fig. 5). The mean difference (bias) (Table 2) is shown by the solid red horizontal line, and the limits of agreement within which 95% of the differences lie are shown by dashed red lines (mean difference ± 1.96 times the standard deviation of the differences). In the difference plots examining the extent of hypertransmission in group 1 (hyperAF rings in SW-AF and NIR-AF images), the values tended to be lower or of similar width as EZ loss. The values reflecting the combined widths of hypoAF and hyperAF measured in NIR-AF and SW-AF images did not cluster around the line of equality (zero); this indicated a systematic difference (bias) in the aforementioned measurements. Specifically, the horizontal line at the mean of the difference was below the 0 line indicating that widths of hypertransmission were typically lower than the width of EZ loss (bias: −453) and the widths of NIR–hypo+hyperAF (bias: −450) and SW–hypo+hyperAF (bias: −552). In the hypertransmission versus SW-hypoAF plot the calculated bias was 38 demonstrating a good agreement among these measurements. The bias calculated for the width of EZ loss versus SW-hypo+hyperAF was also relatively small (bias: −99) suggesting comparatively better agreement than the comparison between EZ and SW-hypoAF (bias: 415). Agreement between the EZ metric and NIR-hypo+hyperAF was also good (bias: 143). The mean differences (bias: 135) for NIR-hypoAF versus SW-hypoAF were either on or above the line of equality (Supplementary Fig. S1); this indicated a trend toward wider hypoautofluorescent lesions in NIR-AF images.

In the Bland-Altman plots associated with group 2 images (hyper-AF ring only in SW-AF images), the negative bias' revealed that the width of hypertransmission was also narrower than the width of EZ loss (bias: −759), the width of NIR-hypoAF (bias: −517) and the width of the zone of SW-hypo+hyperAF (bias: −617). In the plots of EZ loss versus NIR-hypoAF (bias: 241) and EZ loss versus SW-hypo+hyperAF (bias: 141), the values were distributed on both sides of the line of equality (zero) indicating better agreement. In group 2, the width of EZ loss exhibited better agreement when both hypoAF and hyperAF areas in

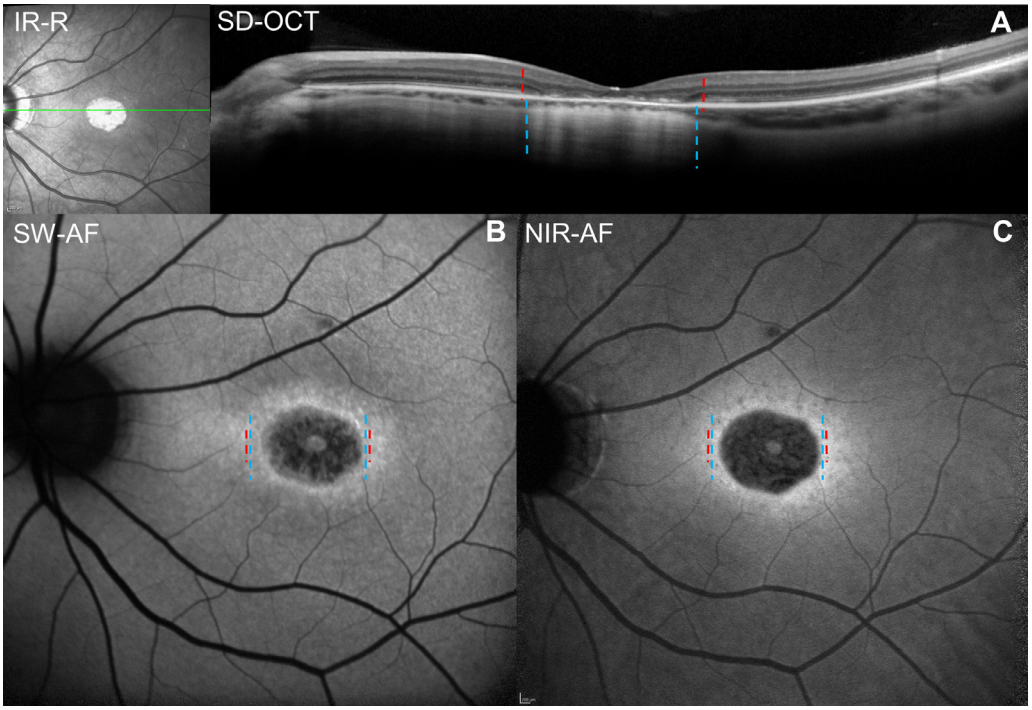

Figure 2. Multimodal fundus images. Group 1; P14. (A) SD-OCT and IR-R. The *green line* in the IR-R image indicates the horizontal axis of the SD-OCT scan. (B) SW-AF, NIR-AF. SW-AF and NIR-AF images exhibit a hyperAF ring surrounding the central hypoAF lesion. The *vertical dashed lines* colocalize in the three imaging modalities; *red*, limits of continuous EZ loss; *blue*, limits of hypertransmission of SD-OCT signal.

SW-AF images were considered (bias: 141) than when the SW-AF hypoAF area alone was measured (bias: 831). The differences between NIR-AF hypoAF and SW-AF hypoAF in group 2 (Supplementary Fig. S1, values on the y axis) were consistently above the zero line; this together with the positive bias of 610 (represented by the red line) indicated that the values for lesion width in NIR-AF images were always larger than the hypoAF lesion width measured in SW-AF images. Bland-Altman plots constructed to analyze group 3 measurements (hyperAF rings are not present) disclosed results similar to groups 1 and 2 when hypertransmission width was examined. Specifically, the horizontal line at the mean of the difference was below the 0 line indicating that hypertransmission measurements were typically lower than the width of EZ loss (bias: −968) and the widths of NIR-hypoAF (bias: −907) and SW-hypoAF (bias: −779). On the other hand, the bias' calculated for the difference between width of EZ loss and width of SW-hypoAF (bias: 246) and NIR-hypoAF (bias: 61) were considerably smaller, indicating better agreement among these modes of measurement of atrophy particularly with respect to NIR-hypoAF.

We used repeated measures ANOVA followed by pair-wise comparisons using Tukey's multiple comparisons test to detect differences ($P < 0.05$). If the P value was >0.05, we assumed the metrics were not different. In Group 1 the comparison of hypertransmission width to EZ loss and hypo+hyperAF in NIR-AF and SW-AF revealed P-values below 0.05 indicating a statistically significant difference among these groups. In contrast, hypertransmission width versus hypoAF measurements in both SW-AF and NIR-AF showed P-values greater than 0.05 indicating no differences. When the width of EZ loss was compared with the combined widths of the hypoAF and hyperAF zones (NIR-hypo+hyper; SW-hypo+hyper) in the SW- and NIR-AF images, the means were found to be similar ($P > 0.9$). On the other hand, the width of EZ loss was significantly larger (EZ vs. SW-hypoAF $P < 0.01$; EZ vs. NIR-hypoAF $P < 0.01$) when EZ loss was compared to the width of the hypoAF zone only.

In group 2 the comparison of widths of hypertransmission with NIR-hypoAF, SW-hypo+hyperAF and EZ loss showed statistically significant differences between these metrics. Interestingly the comparison of the width of hypertransmission versus SW-hypoAF had a P value = 0.8606 indicating similarity between these measured widths. It is important to note that the Bland-Altman plot also revealed a considerably diminished bias in the same comparison. The comparison of the width of EZ loss to NIR-hypoAF and SW-hypo+hyperAF both generated P values >0.05,

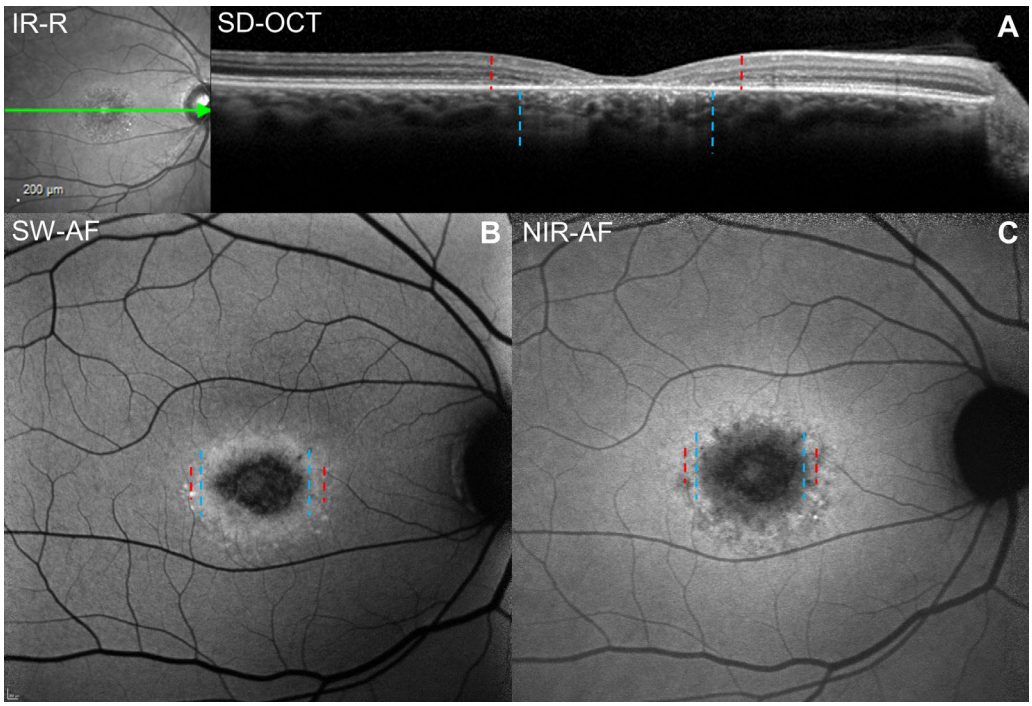

Figure 3. Multimodal fundus images acquired from P9 (group 2). (A) SD-OCT and IR-R. The *green line* in the IR-R image indicates the position of the SD-OCT scan. (B) SW-AF. (C) NIR-AF. In B (SW-AF) the central hypoAF lesion is surrounded by a hyperautofluorescent ring that is not present in the NIR-AF image. The *vertical dashed lines* colocalize in the three imaging modalities; *red*, limits of continuous EZ loss; *blue*, limits of hypertransmission of SD-OCT signal.

indicating absence of differences. The *P* value for EZ loss versus SW-hypoAF was <0.0001 indicating a difference between the two measurements.

In group 3 all *P* values for the width of hypertransmission versus SW-AF, NIR-AF and EZ loss were less than 0.05, indicating that the width of hypertransmission was significantly lower relative to the aforementioned metrics. Conversely, when comparing EZ loss with the width of SW-AF and NIR-AF hypoAF, the *P* values were greater than 0.05.

In summary, using repeated-measures ANOVA followed by pair-wise comparisons we found that all three groups presented with smaller widths of measured hypertransmission relative to the width of EZ loss and smaller widths as compared to visible AF lesions in NIR-AF and SW-AF. Corresponding results were observed using the Bland Altman analysis. When comparing EZ metrics against visible total lesion widths in NIR-AF and SW-AF, all three groups showed *P* values >0.05, indicating good agreement (Table 2). Finally we note that group 3 presented with wider atrophic lesions than groups 1 and 2 and the lesions were wider in group 2 than in group 1.

To determine reliability, a second operator performed all measurements. Reliability between the operators was evaluated by calculating intraclass correlation coefficients (ICC) for hypertransmission (ICC: 0.91, 95% CI, 0.72–0.96), EZ loss (ICC: 0.85, 95% CI, 0.75–0.91), SW-hypoAF (ICC; 0.89, 95% CI, 0.67–0.93), SW-hypo+hyperAF (ICC: 0.91, 95% CI, 0.82–0.96), NIR-hypoAF (ICC: 0.9, 95% CI, 0.76–0.95) and NIR-hypo+hyperAF (ICC: 0.94, 95% CI, 0.17–0.99). ICC values showed good to excellent agreement between the two operators for all the measurements (range, 0.85–0.94). Values less than 0.5 are indicative of poor reliability; values between 0.5 and 0.75 indicate moderate reliability; values ranging from 0.75 to 0.9 indicate good reliability; and values greater than 0.9 indicate excellent reliability.[31]

Discussion

There is a need in cases of macular disease to design interventional studies that include end-point measurements of well-characterized features in retinal images. The size of the central area of atrophy is valued as a critical outcome measure. We show here that imaging modalities provide different measures of the width of atrophy. Specifically, the width of sub-RPE hypertransmission in a horizontal SD-OCT scan through the fovea tended to be narrower than the width of EZ loss.

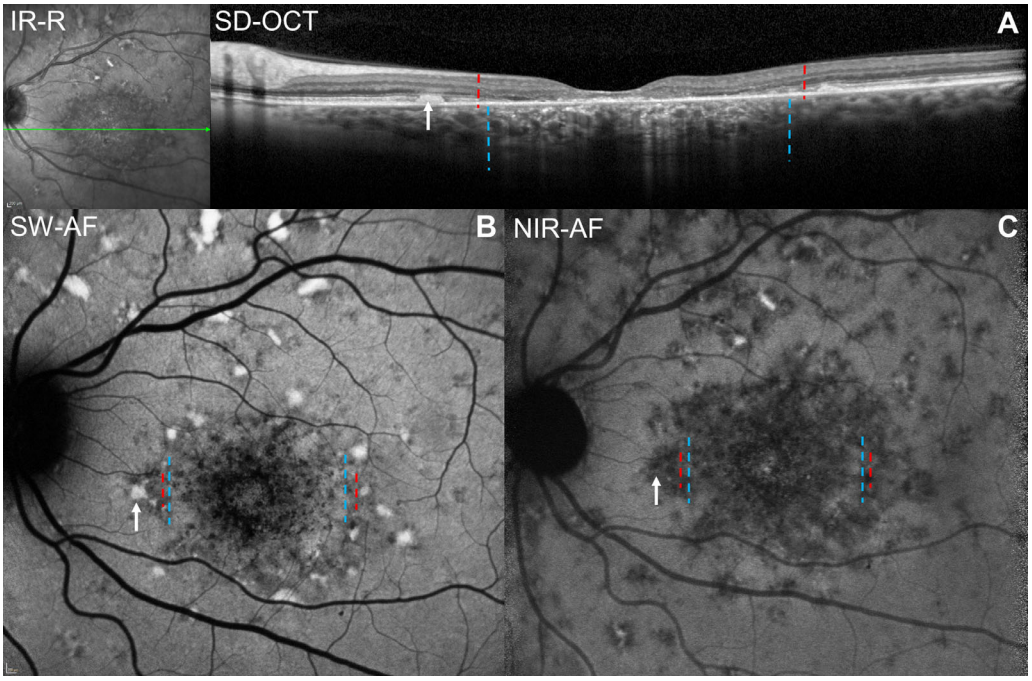

Figure 4. Multimodal images obtained from a patient (P3; group 3). (A) IR-R and SD-OCT. The *green line* in the IR-R image indicates the horizontal axis of the SD-OCT scan. (B) SW-AF. (C) NIR-AF. SW-AF and NIR-AF images exhibit a central hypoautofluorescent (hypoAF) lesion. The positions of the *vertical dashed lines* correspond in the three imaging modalities; *red*, limits of continuous EZ loss; *blue*, limits of hypertransmission of SD-OCT signal. *White arrow* indicates corresponding fleck visible in the three modalities.

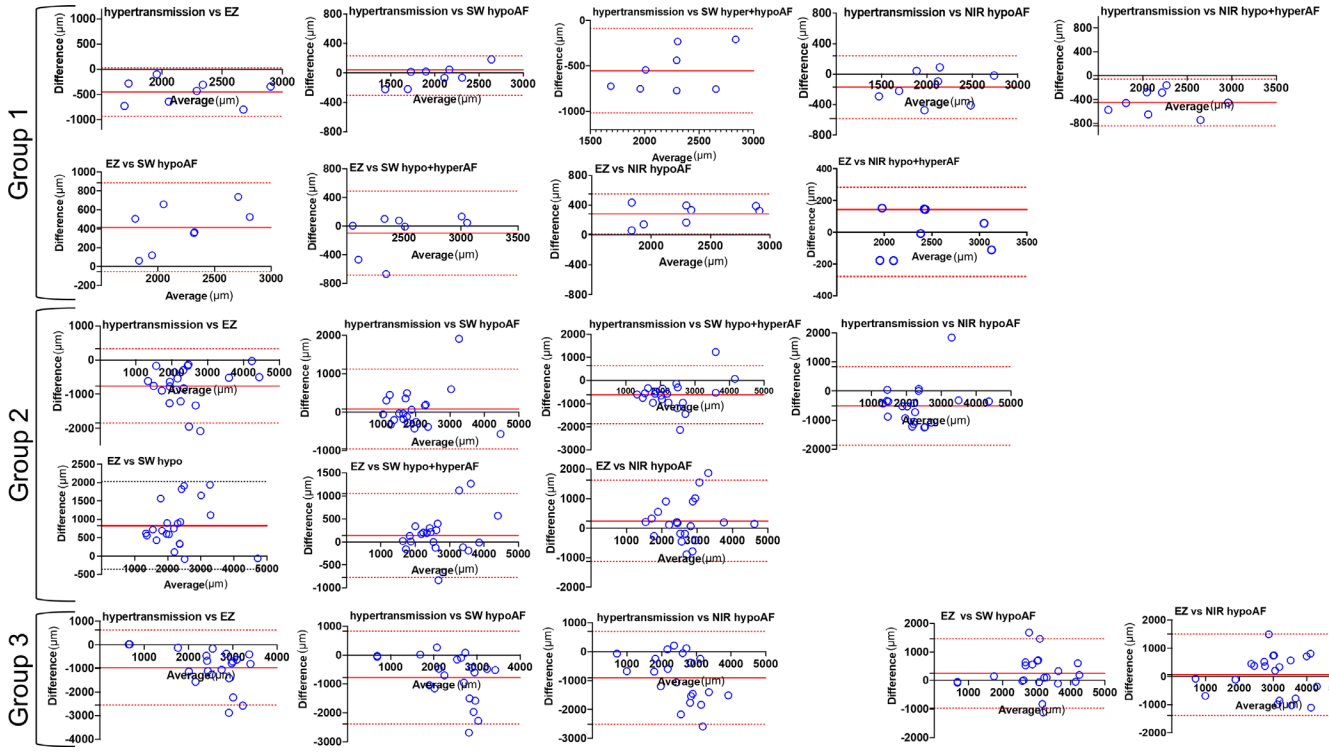

Figure 5. Bland-Altman plots for Groups 1, 2, and 3. The difference between two measurements is plotted as a function of the average of the two measurements. These include measurements of the widths of hypertransmission, widths of EZ loss, and widths of lesions in short wavelength (SW-AF) and near-infrared (NIR-AF) images. In the SW-AF and NIR-AF images atrophic lesions were measured as width of hypoAF or hypo+hyperAF. The mean of the differences is indicated by the *solid red horizontal line* and the 95% limits of agreement by the *dashed lines*. The bias is represented by the gap between zero difference and mean of the differences. Most "means of the differences" lie between −1.96 and +1.96 times the standard deviation of the differences indicating normal distributions.

Table 2. Lesion Measurements and Statistical Analysis

Variables	Mean of 1st Variable (μm)*	Mean of 2nd Variable (μm)*	Bias†	*P* Value‡
Group 1 (8 eyes)				
HyperTM	1978 ± 440			
EZ loss		2432 ± 460	−453	0.0097
SW-hypoAF		2016 ± 336	38	0.959
SW-hypo+hyperAF		2531 ± 335	−552	0.0026
NIR-hypoAF		2151 ± 403	−173	0.2949
NIR-hypo+hyperAF		2429 ± 450	−450	0.0033
EZ loss	2432 ± 460			
SW-hypoAF		2016 ± 336	415	0.0139
SW-hypo+hyperAF		2531 ± 335	−99	0.9244
NIR-hypoAF		2151 ± 403	280	0.0058
NIR-hypo+hyperAF		2429 ± 450	143	>0.9999
NIR-hypoAF	2151 ± 403			
SW-hypoAF		2016 ± 336	135	0.4451
SW-hypo+hyperAF		2531 ± 335	−379	0.0159
NIR-hypo +hyperAF	2429 ± 450			
SW-hypoAF		2016 ± 336	412	0.0072
SW-hypo+hyperAF		2531 ± 335	−102	0.7966
Group 2 (22 eyes)				
HyperTM	2017 ± 886			
EZ loss		2736 ± 830	−759	<0.0001
SW-hypoAF		1905 ± 798	78	0.8606
SW-hypo+hyperAF		2595 ± 711	−617	0.0037
NIR-hypoAF		2515 ± 737	−517	0.0198
EZ loss	2736 ± 830			
SW-hypoAF		1905 ± 798	831	<0.0001
SW-hypo+hyperAF		2595 ± 711	141	0.6236
NIR-hypoAF		2515 ± 737	241	0.6749
NIR-hypoAF	2515 ± 737			
SW-hypoAF		1905 ± 798	610	<0.0001
SW-hypo+hyperAF		2595 ± 711	−80	0.9799
Group 3 (22 eyes)				
HyperTM	2041 ± 674			
EZ loss		3046 ± 995	−968	<0.0001
SW-hypoAF		2800 ± 963	−779	0.0019
NIR-hypoAF		2918 ± 1003	−907	0.003
EZ loss	3046 ± 995			
SW-hypoAF		2800 ± 963	246	0.2716
NIR-hypoAF		2918 ± 1003	61	0.9256
NIR-hypoAF	2918 ± 1003			
SW-hypoAF		2800 ± 963	128	0.4197

*± Standard deviation.
†Calculated as mean difference, Bland Altman plot.
‡Repeated measures ANOVA and Tukey's multiple comparison.

We also found that the width of hypertransmission was narrower than the entire width of abnormal autofluorescence in en face SW- and NIR-AF images. Specifically, in groups 1 and 2 the entire abnormal region included both the hypo-AF and hyper-AF zones and it is the combined width of these two zones that is significantly larger than the width of hypertransmission. In group 3 the entire width of the abnormal autofluorescence consisted of the width of SW-hypoAF and the width of NIR-hypoAF and in both modalities these widths were greater than the width of hypertransmission. Moreover the results confirm that for the purposes of correlating photoreceptor cell changes in SD-OCT scans with atrophy in en face SW- and NIR-AF images, the entire zone of abnormal autofluorescence in SW- and NIR-AF images should be included because, as reported previously,[17,25–27] it is this area that corresponds spatially to the width of EZ loss in horizontal SD-OCT scans.

Differences attributable to imaging modalities were also appreciated in earlier studies. For example, studies reported that the area of RPE atrophy in STGD1 patients was larger in NIR-AF images than in SW-AF images,[17,25–27] whereas the rates of lesion enlargement in the two modalities were similar.[26] HyperAF and hypoAF patterns in NIR-AF and SW-AF have also been compared to SD-OCT findings. For instance, the width of hypoAF areas in NIR-AF images were shown to correlate spatially with the borders of EZ loss.[18,30] Areas outside of dark lesions in SW-AF images have also been evaluated for functional abnormalities.[21] The latter study showed that photoreceptor dysfunction assessed by microperimetry extended peripheral to the dark lesions detected in SW-AF images.[21] The width of EZ loss in OCT scans has been compared to atrophy in NIR-AF and SW-AF findings in a study which measured abnormal reflectivity in en face slab images generated from B-scans acquired by wide-field swept-source OCT.[17] The area of the central hyperreflective zone attributable to RPE atrophy in the sub-RPE slab was in agreement with the hypoAF SW-AF area but both underestimated RPE atrophy based on the area of hypoAF in NIR-AF images.[17] The area of abnormal reflectivity attributable to EZ loss in the inner segment/outer segment (IS/OS) slab corresponded to the zone of combined hypoAF and hyperAF in SW-AF images.

We found that widths of sub-RPE hypertransmission in SD-OCT scans were smaller than the width of EZ loss in the scans. NIR-AF imaging has not previously been compared with hypertransmission detected in SD-OCT scans, and we found that the widths of hypertransmission were smaller than the widths of abnormal autofluorescence determined using signals from melanin (NIR-AF) and lipofuscin bisretinoid (SW-AF) in RPE. In its favor, however, hypertransmission in horizontal B-scans is reported to be reliably detected by reading centers even in the case of small areas.[32] Sub-RPE hypertransmission of OCT signal and disruption of the ellipsoid zone (EZ) of photoreceptor inner segments (EZ loss) are both indicative of outer retinal changes. However, EZ loss signifies degenerative changes in photoreceptor cells whereas hypertransmission of OCT signal depends on a loss of reflectivity in the RPE.[33] Hypertransmission into the choroid is a result of reduction or loss of reflectance by RPE melanin in association with attenuation, interruptions in, or complete loss of the RPE-monolayer and need not be associated with definite photoreceptor cell degeneration.[29,34] Hypertransmission can likely be thwarted by hyperreflective debris not yet cleared and may co-localize with the darkest and most central zone of hypoAF in SW-AF images.[26]

Rings of hyperAF surrounding dark atrophy in SW-AF images of STGD1 patients are frequently observed.[25] At these locations, NIR-AF derived from melanin is typically reduced; this suggests that at the position of these SW-AF rings, RPE cells cannot fully account for the SW-AF. An alternate source is AF emitted directly from abnormally enhanced formation of bisretinoid lipofuscin in impaired photoreceptors, the cells in which these bisretinoid lipofuscin fluorophores are synthesized.[25]

We found that hyperAF rings in NIR-AF images were only observed in group 1. We also noted that the total lesion size increased between Groups 1, 2 and 3. Thus these phenotypes are likely indicative of disease progression with the phenotypes reflecting different stages of disease. Moreover since the region of hypoAF is also distinctly larger in the NIR-AF images than in SW-AF in Groups 1 and 2, the changes in NIR-AF probably occur in advance of SW-AF.

Nevertheless, although the signal from NIR-AF originates primarily from RPE melanin, the reason underlying hyperAF in NIR-AF images is not fully understood. It has been suggested that NIR-AF may be increased because of the changes in the distribution of lipofuscin-containing organelles relative to melanosomes allowing the lipofuscin to modulate NIR-AF signal from melanin.[25] An alternative explanation of increased AF in both imaging modalities could be the superimposition of RPE cells and cellular fragments in the periphery of the lesion.[35] Other explanations might be apical displacement of intracellular melanin granules or formation of derivatives such as melano-lipofuscin and oxidized melanin.[18] One might consider whether a window defect contributes to hyperAF in NIR-AF images. Near-infrared light is

associated with low levels of scattering, and absorption by the major optical absorbers in tissues (hemoglobin < 650 nm; and water >900 nm) is low in the spectral range of 650 to 900 nm, which is in the wavelength range of NIR-AF images (787 nm excitation).[36,37] Thus, in the case of the NIR-AF signal, it is unlikely that a window defect would be created.

One limitation of this study is that it was not designed to observe progression in individual patients. We also acknowledge the relatively small numbers of patients in Group 1. Inclusion in all modalities was limited to images with clearly defined phenotypes. Moreover, in healthy eyes, the area of higher melanin optical density that presents as the zone of brightness in NIR-AF extends within an area 8° in diameter and corresponds to the area of higher melanin optical density that is observed in color and blue/SW-AF images. It can be difficult to distinguish the normal brightness in this area from abnormal hyperNIR-AF (Fig. 3).

Because the disease-causing genetic variant in *ABCA4* is expressed in photoreceptor cells, although the product of ABCA4-deficiency, bisretinoid lipofuscin, accumulates in RPE cells, questions have beset investigators regarding the sequence of cellular involvement in the disease process. Such a determination requires careful interpretation of multimodal images. We observed here, as before, that the area of hypoAF in SW-AF images underestimates atrophy. Conversely, the entire area of abnormal autofluorescence in en face SW-AF images corresponds spatially to the loss of RPE melanin signal as detected by NIR-AF and to the area of EZ loss.[13,17,27]

Acknowledgments

Supported by grants from the National Eye Institute/NIH EY024091, EY028954, EY009076 and P30 EY019007; from Foundation Fighting Blindness; and a grant from Research to Prevent Blindness to the Department of Ophthalmology, Columbia University.

Disclosure: **R. Parmann,** None; **S.H. Tsang,** None; **J. Zernant,** None; **R. Allikmets,** None; **V.C Greenstein,** None; **J.R. Sparrow,** None

References

1. Fujinami K, Sergouniotis PI, Davidson AE, et al. Clinical and molecular analysis of Stargardt disease with preserved foveal structure and function. *Am J Ophthalmol*. 2013;156:487–501 e481.
2. Cideciyan AV, Aleman TS, Swider M, et al. Mutations in ABCA4 result in accumulation of lipofuscin before slowing of the retinoid cycle: a reappraisal of the human disease sequence. *Hum Mol Genet*. 2004;13:525–534.
3. Nassisi M, Mohand-Said S, Andrieu C, et al. Prevalence of ABCA4 deep-intronic variants and related phenotype in an unsolved "one-hit" cohort with Stargardt disease. *Int J Mol Sci*. 2019;20(20):5053.
4. Lambertus S, Bax NM, Fakin A, et al. Highly sensitive measurements of disease progression in rare disorders: Developing and validating a multimodal model of retinal degeneration in Stargardt disease. *PLoS One*. 2017;12:e0174020.
5. Jayasundera T, Rhoades W, Branham K, Niziol LM, Musch DC, Heckenlively JR. Peripapillary dark choroid ring as a helpful diagnostic sign in advanced stargardt disease. *Am J Ophthalmol*. 2010;149:656–660.e652.
6. Lois N, Holder GE, Fitzke FW, Plant C, Bird AC. Intrafamilial variation of phenotype in Stargardt macular dystrophy-fundus flavimaculatus. *Invest Ophthalmol Vis Sci*. 1999;40:2668–2675.
7. Lois N, Halfyard AS, Bird AC, Holder GE, Fitzke FW. Fundus autofluorescence in Stargardt macular dystrophy-fundus flavimaculatus. *Am J Ophthalmol*. 2004;138:55–63.
8. Delori FC, Staurenghi G, Arend O, Dorey CK, Goger DG, Weiter JJ. In vivo measurement of lipofuscin in Stargardt's disease–Fundus flavimaculatus. *Invest Ophthalmol Vis Sci*. 1995;36:2327–2331.
9. Burke TR, Duncker T, Woods RL, et al. Quantitative fundus autofluorescence in recessive stargardt disease. *Invest Ophthalmol Vis Sci*. 2014;55:2841–2852.
10. Fishman GA, Stone EM, Grover S, Derlacki DJ, Haines HL, Hockey RR. Variation of clinical expression in patients with Stargardt dystrophy and sequence variations in the ABCR gene. *Arch Ophthalmol*. 1999;117:504–510.
11. Querques G, Leveziel N, Benhamou N, Voigt M, Soubrane G, Souied EH. Analysis of retinal flecks in fundus flavimaculatus using optical coherence tomography. *Br J Ophthalmol*. 2006;90:1157–1162.
12. Cukras CA, Wong WT, Caruso R, Cunningham D, Zein W, Sieving PA. Centrifugal expansion of fundus autofluorescence patterns in Stargardt disease over time. *Arch Ophthalmol*. 2012;130:171–179.
13. Sparrow JR, Marsiglia M, Allikmets R, et al. Flecks in recessive Stargardt disease: Short-wavelength autofluorescence, near-infrared

autofluorescence, and optical coherence tomography. *Invest Ophthalmol Vis Sci*. 2015;56:5029–5039.
14. Tanna P, Georgiou M, Aboshiha J, et al. Cross-sectional and longitudinal assessment of retinal sensitivity in patients with childhood-onset Stargardt disease. *Transl Vis Sci Technol*. 2018;7:10.
15. Keilhauer CN, Delori FC. Near-infrared autofluorescence imaging of the fundus: visualization of ocular melanin. *Invest Ophthalmol Vis Sci*. 2006;47:3556–3564.
16. Kellner S, Kellner U, Weber BH, Fiebig B, Weinitz S, Ruether K. Lipofuscin- and melanin-related fundus autofluorescence in patients with ABCA4-associated retinal dystrophies. *Am J Ophthalmol*. 2009;147:895–902.
17. Greenstein VC, Nunez J, Lee W, et al. A comparison of en face optical coherence tomography and fundus autofluorescence in Stargardt disease. *Invest Ophthalmol Vis Sci*. 2017;58:5227–5236.
18. Muller PL, Birtel J, Herrmann P, Holz FG, Charbel Issa P, Gliem M. Functional Relevance and Structural Correlates of Near Infrared and Short Wavelength Fundus Autofluorescence Imaging in ABCA4-Related Retinopathy. *Transl Vis Sci Technol*. 2019;8:46.
19. Paavo M, Lee W, Allikmets R, Tsang S, Sparrow JR. Photoreceptor cells as a source of fundus autofluorescence in recessive Stargardt disease. *J Neurosci Res*. 2019;97:98–106.
20. Ervin AM, Strauss RW, Ahmed MI, et al. A workshop on measuring the progression of atrophy secondary to Stargardt Disease in the ProgStar Studies: Findings and lessons learned. *Transl Vis Sci Technol*. 2019;8:16.
21. Sunness JS, Ifrah A, Wolf R, Applegate CA, Sparrow JR. Abnormal visual function outside the area of atrophy defined by short-wavelength fundus autofluorescence in Stargardt disease. *Invest Ophthalmol Vis Sci*. 2020;61:36.
22. Fujinami K, Lois N, Mukherjee R, et al. A longitudinal study of Stargardt disease: Quantitative assessment of fundus autofluorescence, progression, and genotype correlations. *Invest Ophthalmol Vis Sci*. 2013;54:8181–8190.
23. Kong X, Strauss RW, Michaelides M, et al. Visual acuity loss and associated risk factors in the Retrospective Progression of Stargardt Disease Study (ProgStar Report No. 2). *Ophthalmology*. 2016;123:1887–1897.
24. Strauss RW, Munoz B, Ho A, et al. Progression of Stargardt disease as determined by fundus autofluorescence in the Retrospective Progression of Stargardt Disease Study (ProgStar Report No. 9). *JAMA Ophthalmol*. 2017;135:1232–1241.
25. Duncker T, Marsiglia M, Lee W, et al. Correlations among near-infrared and short-wavelength autofluorescence and spectral-domain optical coherence tomography in recessive Stargardt disease. *Invest Ophthalmol Vis Sci*. 2014;55:8134–8143.
26. Jauregui R, Nuzbrokh Y, Su PY, et al. Retinal pigment epithelium atrophy in recessive Stargardt disease as measured by short-wavelength and near-infrared autofluorescence. *Transl Vis Sci Technol*. 2021;10:3.
27. Greenstein VC, Schuman AD, Lee W, et al. Near-infrared autofluorescence: Its relationship to short-wavelength autofluorescence and optical coherence tomography in recessive Stargardt disease. *Invest Ophthalmol Vis Sci*. 2015;56:3226–3234.
28. Kong X, Strauss RW, Cideciyan AV, et al. Visual acuity change over 12 months in the prospective Progression of Atrophy Secondary to Stargardt Disease (ProgStar) Study: ProgStar Report number 6. *Ophthalmology*. 2017;124:1640–1651.
29. Shi Y, Yang J, Feuer W, Gregori G, Rosenfeld PJ. Persistent hypertransmission defects on en face OCT imaging as a stand-alone precursor for the future formation of geographic atrophy [published online ahead of print February 19, 2021]. *Ophthalmol Retina*, doi:10.1016/j.oret.2021.02.004.
30. Duncker T, Marsiglia M, Lee W, et al. Correlations amongst near-infrared and short-wavelength autofluorescence and spectral domain optical coherence tomography in recessive Stargardt disease. *Invest Ophthalmol Vis Sc*. 2014;55:8134–8143.
31. Koo TK, Li MY. A guideline of selecting and reporting intraclass correlation coefficients for reliability research. *J Chiropr Med*. 2016;15:155–163.
32. Wu Z, Pfau M, Blodi BA, et al. OCT signs of early atrophy in age-related macular degeneration: Interreader agreement: Classification of Atrophy Meetings Report 6 [published online ahead of print March 23, 2021]. *Ophthalmol Retina*, doi:10.1016/j.oret.2021.03.008.
33. Jaffe GJ, Chakravarthy U, Freund KB, et al. Imaging features associated with progression to geographic atrophy in age-related macular degeneration: Classification of Atrophy Meeting Report 5. *Ophthalmol Retina*. 2021;5:855–867.
34. Guymer RH, Rosenfeld PJ, Curcio CA, et al. Incomplete retinal pigment epithelial and outer retinal atrophy in age-related macular degeneration: Classification of Atrophy Meeting Report 4. *Ophthalmology*. 2020;127:394–409.

35. Sparrow JR, Yoon K, Wu Y, Yamamoto K. Interpretations of fundus autofluorescence from studies of the bisretinoids of retina. *Invest Ophthalmol Vis Sci*. 2010;51:4351–4357.
36. Wang J, Li H, Tian G, Deng Y, Liu Q, Fu L. Near-infrared probe-based confocal microendoscope for deep-tissue imaging. *Biomed Opt Express*. 2018;9:5011–5025.
37. Harada K, Miwa M, Fukuyo T, Watanabe S, Enosawa S, Chiba T. ICG fluorescence endoscope for visualization of the placental vascular network. *Minim Invasive Ther Allied Technol*. 2009;18:1–5.